Suppressed ion migration in powder-based perovskite thick films using an ionic liquid

Philipp Ramming[1], Nico Leupold[2], Konstantin Schötz[1], Anna Köhler[1], Ralf Moos[2], Helen Grüninger[3], Fabian Panzer[1*]

[1] Soft Matter Optoelectronics, University of Bayreuth, Bayreuth 95440, Germany.

[2] Department of Functional Materials, University of Bayreuth, Bayreuth 95440, Germany

[3] Institute for Molecules and Materials, Radboud University, Heyendaalseweg 135, 6525 AJ Nijmegen, The Netherlands

Corresponding Author:

[*]E-Mail: fabian.panzer@uni-bayreuth.de

Keywords: passivation, $MAPbI_3$, $BMIMBF_4$, powder pellet, hysteresis, dark current

Abstract

While solution-processed halide perovskite thin films caused enormous attention when used in solar cells, thick films prepared by compressing perovskite powders are considered promising candidates for the next generation of X-ray detectors. However, X-ray detectors based on such powder-pressed perovskites typically suffer from relatively high dark currents, which were attributed to be caused by ion migration. Here we show that the dark current in 800 µm thick powder-pressed $MAPbI_3$-pellets can be reduced by a factor of 25 when using a passivated powder. The passivation was achieved by adding 1 mol% of the ionic liquid (IL) $BMIMBF_4$ to the precursors MAI and PbI_2 during the mechanochemical synthesis of the $MAPbI_3$ powder. NMR verified the presence of the IL, and its impact on the excited state recombination dynamics was manifested in an increase in the photoluminescence (PL) intensity and a decrease in the monomolecular (trap-assisted) recombination rate, both by about one order of magnitude. By measuring the migration of a PL quenching front upon application of a field in a microscope, we determine an ionic diffusivity in the typical range of iodine vacancies in the non-passivated pellet. At the same time, we observe no such PL quenching front in the passivated pellet. Concomitantly, dark I-V curves are hysteresis-free, and light-soaking effects are absent, in contrast to non-passivated pellets. Thus, our work demonstrates the effect on the optical and electrical properties when passivating mechanochemically synthesized halide perovskite powders using an IL, which will facilitate the further development of powder-based perovskite X-ray detectors.

1. Introduction

Halide perovskites have undergone a spectacular development in recent years so that perovskite solar cells are now on the edge of commercialization.[1] However, in the shadow of the solar cells, also other perovskite-based optoelectronic applications have emerged, such as LEDs,[2] memristors, and especially detectors for high-energy radiation, like X-ray or gamma-rays.[3-6]

The developments of the latter are particularly noteworthy. For solar cells, lab efficiencies are now on par with the commercially established competitor, i.e., silicon.[7] However, when used for direct-conversion X-ray detectors, halide perovskites actually outperform commercially used semiconductor materials such as a-Se regarding their sensitivity.[6, 8] Highly efficient perovskite X-ray detectors have so far been realized in the laboratory using high-quality single crystals.[9, 10] However, only sophisticated methods allow the growth of perovskite single crystals in a thick-film geometry that is required for commercialization.[11]

An attractive alternative in terms of process technology is to transfer perovskites in powder form into thick layers, e.g., by compressing the powder, and to use these thick layers in X-ray detectors.[12] It is possible to produce halide perovskite powders, even on the kilogram scale per batch, for example by mechanochemical synthesis via ball milling.[13-15] However, detectors based on perovskite powder layers typically exhibit significantly higher dark currents than their single crystal counterpart devices.[16, 17] These high currents limit the detector sensitivity and they often exhibit instability over time, which is a current hurdle for commercialization of perovskite X-ray detectors.[16] It has been suggested that mobile ions are responsible for the high dark current,[12, 16] and in the past attempts have been made to reduce and temporally stabilize the dark current, e.g., by using low-dimensional perovskite materials.[18, 19]

In the field of perovskite solar cells, reducing ion migration has been a focus of interest for quite some time.[20-23] For this purpose, various strategies were applied, such as

compositional engineering,[24] the use of low dimensional perovskite materials,[25] interface modifications[26] and in particular the introduction of additives such as potassium. While some of the additives, such as choline chloride, mainly showed a passivating effect at the interface between the perovskite and the transport layer,[27] ionic liquids (IL) have recently been shown to passivate the bulk of the perovskite layer.[28] In this context, the term "passivation" refers to chemical passivation leading to a reduction in defect trap density.[29] This resulted in improved power conversion efficiencies and excellent stabilities of solar cells fabricated from such passivated perovskite thin films.[30-32] For mechanochemically synthesized perovskite powders, we recently demonstrated successful chemical passivation by adding potassium iodide to the milling process.[33] This reduced the non-radiative decay and led to improved power conversion efficiency of solar cells, when the passivated powder was dissolved and used as stock solution in the solution processing.[33]

However, it is not yet clear whether the defect-passivating effects resulting from adding an organic compound, as it is a promising strategy in case of perovskite thin films for solar cells, also apply to powder-pressed thick films. This is, however, crucial for highly-efficient powder-based X-ray detectors.

In this work, we investigate whether a successful reduction of the defect trap density and a subsequent reduction of the dark current can be achieved in powder-based perovskite thick films. We approach this by directly adding the ionic liquid 1-butyl-3-methylimidazolium tetrafluoroborate ($BMIMBF_4$) to the precursors of the model halide perovskite methylammonium lead iodide ($MAPbI_3$) during the mechanochemical synthesis. The resulting passivated powder is then pressed into a thick film. We systematically investigate the luminescence and charge transport properties of non-passivated and passivated powder pellets using various optical and electrical measurement methods. With the addition of the IL, we find a suppressed light soaking effect and a significant reduction of the non-radiative recombination rate in the powder pellets, corresponding to a reduced trap density. By photoluminescence (PL) microscopy investigations, we can identify a suppression of ion migration leading to hysteresis-free IV

curves of the passivated powder pellets. In particular, the suppressed ion migration results in a significant reduction and substantially increased long-term stability of the dark currents. Our work thus demonstrates an important strategy to better exploit the optoelectronic potential of powder-pressed pellets in the future.

2. Results and Discussion

We mechanochemically synthesized $MAPbI_3$ powder by ball milling, as described in more detail in ref 33. In brief, the reactant powders PbI_2 and methylammonium iodide (MAI) are placed in a milling jar, where milling balls and a small amount of cyclohexane, used as milling agent, are present. During planetary ball milling, $MAPbI_3$ synthesis is enabled by the mechanical energy release when the milling balls are impinging on the reactant powders at the inner walls of the milling jar (Fig. 1a). We prepared one batch of non-passivated $MAPbI_3$ powder (referred to as "reference") and in parallel, under the same process conditions, yet with 1 mol% $BMIMBF_4$ added to the milling jar, a second batch of $MAPbI_3$ powder (referred to as "passivated").

The X-ray diffraction (XRD) pattern for both the reference and the passivated powder show only peaks associated with $MAPbI_3$ in the tetragonal phase (Fig. 1b).[34] In particular, we cannot observe any additional peaks, e.g., at 12.6°, due to the presence of crystalline PbI_2.[35] This indicates that even when the IL is added, the $MAPbI_3$ prepared by the mechanochemical synthesis remains completely phase pure, at least with respect to the sensitivity achievable by XRD.

Complementary to the XRD experiments, we performed high-resolution, solid-state ^1H magic angle spinning (MAS) nuclear magnetic resonance (NMR) experiments to identify and to quantify the ionic liquid in our passivated powder sample (Fig. 1c). While the full ^1H MAS NMR spectrum is shown in Fig. S1, a magnified section on the low-intensity ^1H

signals is depicted in Fig. 1c. The ^{1}H chemical shifts of these signals, indicated by colored vertical bars in Fig. 1c, are in good agreement with reported values for $BMIMBF_4$.[36] Furthermore, a quantitative analysis of the low-intensity ^{1}H signals of $BMIMBF_4$ relative to the two strong resonances for the NH_3 and the CH_3 group of $MAPbI_3$ indicates that an amount of about 0.8 mol% IL is present in the sample. This is in good agreement with the amount of 1 mol% that was added in the milling process.

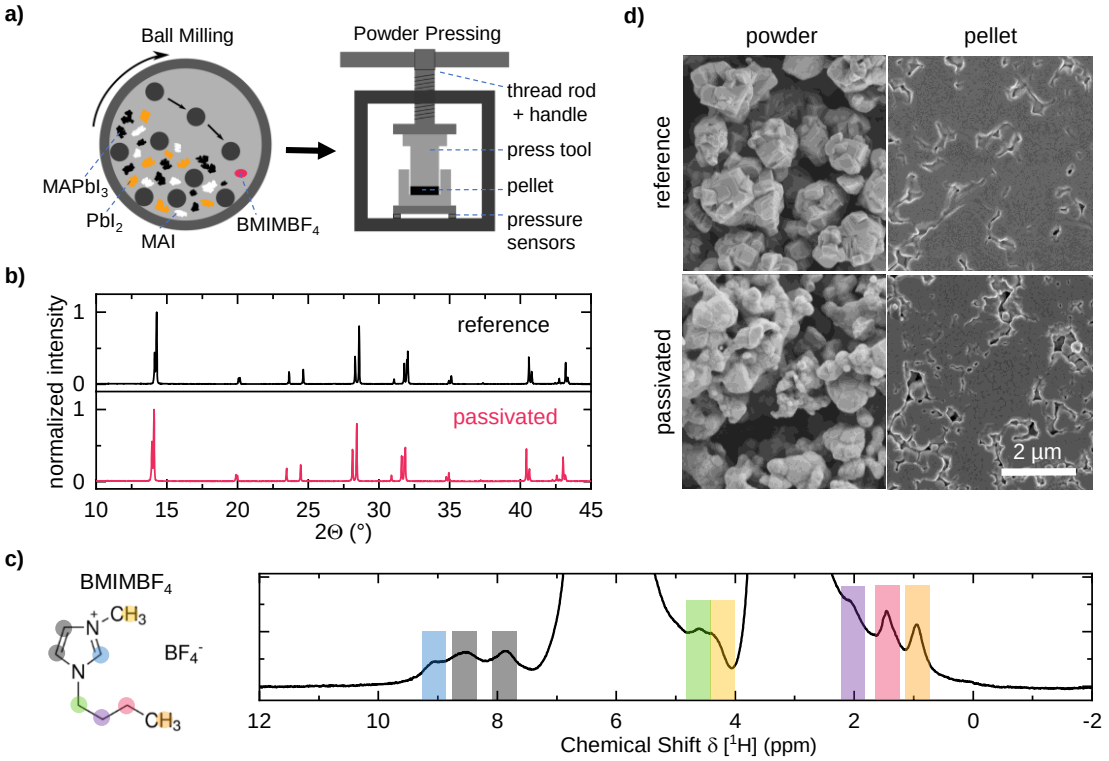

Fig. 1 (a) Schematic illustration of the mechanochemical synthesis of $MAPbI_3$ powder by ball milling and the subsequent pressing step using a mechanical press. For the passivated $MAPbI_3$ powder, 1 mol% $BMIMBF_4$ is added to the MAI and PbI_2 before milling. (b) XRD patterns of the reference and the passivated powder containing the ionic liquid. (c) Chemical structure of $BMIMBF_4$ together with ^{1}H NMR spectra of the passivated powder. The corresponding H-Atoms of the $BMIMBF_4$ in the spectrum are highlighted as colored bars. (d) SEM images of the reference and passivated powder and corresponding powder-pressed pellet surfaces. The scale bar applies to all four images.

We pressed ~0.8 mm thick pellets (Fig. S2 for images) by filling the powders in a mold and compacted them using a homemade mechanical press (Fig. 1a), which is described in more detail in Ref 37. As the NMR measurement has already confirmed the presence of the IL, the lack of a detectable signal in EDX indicates that there are no local accumulations of IL in the pellet but that the IL is homogeneously distributed within the pellet (Fig. S3). Fig. 1d shows top view scanning electron microscopy (SEM) images of both powder and pellet of the reference and the IL passivated $MAPbI_3$ samples (see Fig. S4 for additional images). From this, it is evident that both the morphology of the powder and of the pellet surface do not change significantly by adding IL in the milling process. Rather, both powders exhibit the typical morphology known from previous work, with powder particle sizes in the range of 300 - 800 nm,[33] and mainly compact surfaces after pressing at 100 MPa at room temperature for about 30 minutes.[37] Thus, we conclude that the IL added during ball milling is present in the $MAPbI_3$ powder in the expected amount and leaves the synthesis and the morphology of the $MAPbI_3$ powder unchanged.

To investigate whether the IL reduces the non-radiative decay in the mechanochemically synthesized $MAPbI_3$ powder, we characterized the reference and passivated pellets using PL measurements. PL is well suited for this purpose,[38] since charge carrier recombination in lead halide perovskites can be described by the rate equation,[39]

$$\frac{dn}{dt} = -k_1 n - k_2 n^2 - k_3 n^3, \qquad (1)$$

with n being the photoinduced charge carrier density, k_1 is the rate constant for monomolecular (trap-assisted) recombination, k_2 is the rate constant for bimolecular recombination, and k_3 that for Auger-recombination. In lead halide perovskites, k_2 and k_3 can be considered to be material constants and are thus sample-independent, while k_1 depends on the trap density of the investigated sample. Note that in eqn (1), electron and hole density are assumed to be equal, and charge carrier diffusion and photon recycling

are neglected (see SI section S1 and Fig. S5 for details). Further, k_1 and k_3 are non-radiative, while k_2 is radiative in halide perovskites. The PL quantum yield at a given carrier density is therefore determined by,[40]

$$\Phi_{PL}(n) \propto \frac{k_2 n}{k_1 + k_2 n + k_3 n^2} . \quad (2)$$

Thus, for low to medium charge carrier densities (i.e., $k_2 n + k_3 n^2$ is not significantly larger than k_1), an increase in PL intensity under identical experimental conditions is due to a reduction in k_1.[40] The PL measurements presented in this work are carried out in such a low to medium charge carrier density regime, where we used an excitation fluence that corresponds to a charge carrier density of about 10^{16} cm^{-3}.[41]

Fig. 2a shows the steady-state PL of the reference (black line) and the passivated pellet (red line), both measured in the same experimental geometry, i.e., in the focal plane of a PL microscopy setup (see experimental section for details). The PL intensity of the passivated pellet is increased by more than one order of magnitude compared to the reference pellet. Fig. 2b shows the normalized time-resolved PL (TRPL) curves of the reference (black) and the passivated pellet (red), together with fits (blue line) of simulated transient PL decay curves using eqn (1). The PL decay is significantly slower in the passivated pellet than in the reference pellet. To fit the measured transients, we set k_2 = 6.8×10^{-10} cm^3s^{-1} and k_3 = 10^{-28} cm^6s^{-1}, in accordance with literature,[42] and estimated the initial charge carrier density $n(t=0)$ based on the laser fluence used in the experiments (see Experimental section and Supporting Information section S1). From the fit, we obtain $k_{1,ref}$ = 2.2×10^7 s^{-1} for the reference sample and $k_{1,pass}$ = 3.0×10^6 s^{-1} for the passivated sample, i.e., the monomolecular decay rate is nearly one order of magnitude lower. This ten-fold reduced value of $k_{1,pass}$ indicates a concomitantly reduced trap density in the $MAPbI_3$ powder due the addition of the IL.

To conduct the TRPL measurements, both samples were exposed to the excitation pulse only briefly (about 10 s). However, when the samples were exposed to the exciting laser

for a longer period, we observed that the PL intensity of the reference sample changed. To investigate this further, we excited the pellets with the excitation laser of our TRPL setup, i.e., with 68 ps laser pulses at a frequency of 1 MHz under ambient conditions. Fig. 2c shows the evolution of PL intensity within the first 10 minutes of illumination for the reference and the passivated pellet. The PL intensity of the reference sample increases by about 25 % in the first 90 seconds and decreases to 55 % of the initial value thereafter. In contrast, no initial PL increase occurs in the passivated sample, and the PL intensity drops only slowly during the 10 minutes of illumination to about 96 % of the initial value.

A temporal increase in PL intensity during illumination of halide perovskites is well known and has been referred to as "light soaking effect".[43] This light soaking effect was found to be more pronounced in samples with relatively high non-radiative decay rates, i.e., relatively high trap densities. Motti et al. systematically investigated the light soaking effect and attributed an initial PL increase to light-induced annihilation of iodine Frenkel defect pairs.[44] Furthermore, they associate a PL intensity drop over time with the formation of I_2, which is formed when two iodide ions come together in the perovskite. For both the Frenkel Pair annihilation and the I_2 formation process, ion migration was found to play a crucial role, so that accordingly, light soaking was linked to ion migration in the perovskite.[43] We consider that this process might also account for the PL decrease in the reference pellet in Fig. 2c. The time scale of the light soaking effect, i.e., seconds to minutes, is consistent with the time scale of ion migration. It is also significantly larger than the time scale of other effects such as electronic transport and recombination or trap filling, which occur in the range of 100 ns – 100 ms.[44]

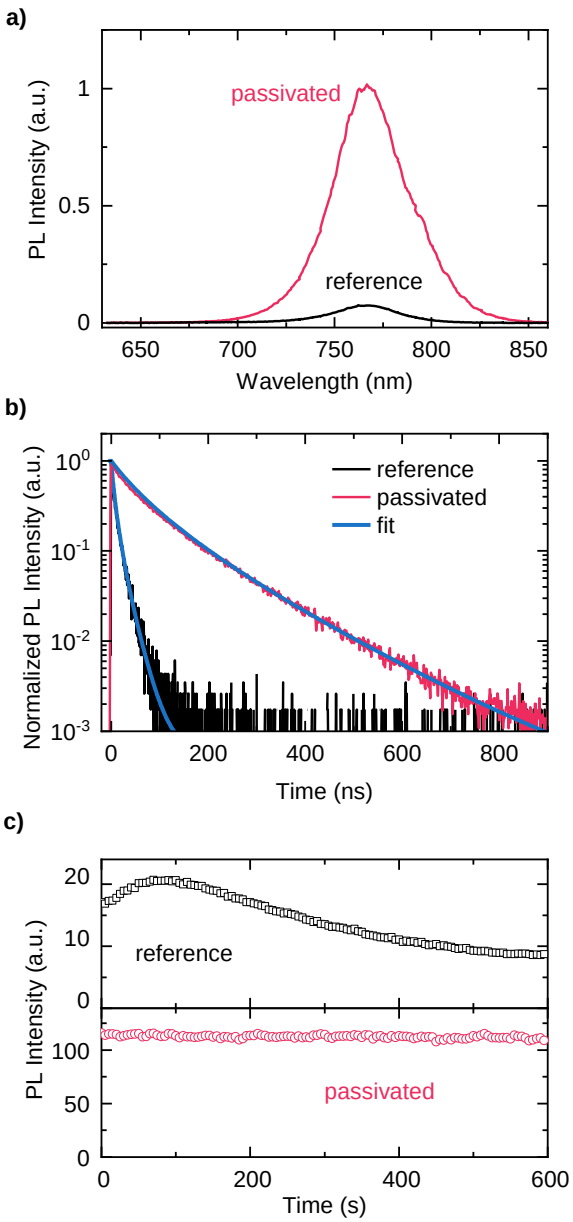

Fig. 2 (a) Steady-state PL spectra of the reference (black) and passivated (red) pellets normalized to the maximum intensity of the passivated pellet. (b) Time-resolved photoluminescence decay curves with fits based on eqn (1) (blue lines). A pulsed laser illuminated the pellets with 1 MHz repetition rate, a wavelength of 560 nm, and a fluence of 0.1 μJ/cm^2 for a total of 10 seconds. An alternative version of (b) to fully represent the baselines and the instrument response function is provided in Fig. S5 (c) Time-trace of the PL intensity for illumination conditions as in (b).

DeQuillets et al. associate the migration of ions out of the illuminated region with the light soaking effect, and by time-dependent PL experiments at different temperatures, they found a corresponding activation energy of about 0.2 eV.[45] This value agrees well with the typical activation energies of 0.1 - 0.3 eV for iodine migration in $MAPbI_3$.[46-48] Furthermore, a significantly reduced light soaking effect was found when passivating mixed perovskites with potassium, consistent with our results.[38] To summarize the findings of Fig. 2, we observe an increase in PL intensity and lifetime upon inclusion of the IL in the powder, as well as an absence of any light-soaking effect. We interpret this as an indication for the chemical passivation of defect traps by the IL.

In passing we note that we have introduced solid potassium into the milling process of $MAPbI_3$ in a previous work leading to a passivation of the perovskite powder.[33] In addition, Abdi-Jalebi et al. used the same potassium salts for the passivation of halide perovskite thin films, which was also accompanied by an inhibition of halide migration.[38] Therefore, the liquid form of $BMIMBF_4$ appears not to be necessary to achieve passivation of the perovskite.

To further clarify whether the temporal PL changes in the reference pellet in Fig. 2 are due to ion migration and whether it is reduced by passivation, we investigate our pellets by PL microscope measurements under an applied electric field. PL imaging microscopy has proven in recent years to be a valuable method to directly monitor and study ion migration in halide perovskites.[49, 50] Thus, we evaporated Au-electrodes, laterally arranged on top of the reference and IL passivated pellets. Fig. 3a shows PL microscopy images from the top surface of the pellet between the electrodes at the beginning, 50 s, and 165 s after applying an electric field of 67 V/cm.

The reference pellet shows a relatively homogeneous PL intensity throughout the 150 μm wide channel at t = 0 s. After applying the electric field, the PL intensity reduces in the area along the positive electrode. Over time, the area with the reduced PL intensity

expands so that a dark front moves towards the negative electrode. This dark front reaches the center of the channel after approx. 50 s. After 165 s, the area of the reduced PL extends over the entire width of the channel. Concomitantly the PL intensity in the vicinity of the positive electrode appears to become brighter again. PL brightening in the vicinity of the electrode, was also identified in some samples by Li et al..[51] They suggested that the additional vacancies annihilate with iodine interstitials and thus reduce non-radiative recombination of electrons and holes.

Fig. 3b shows the temporal evolution of the PL intensities averaged over 10 µm thick horizontal stripes parallel to the electrodes, along the positive electrode, in the middle of the channel, and along the negative electrode (as indicated in Fig. 3a by the colored stripes for the 0 s passivated sample). For each position, the PL intensity is normalized to the value at t = 0 s. For the reference sample, it is evident that the PL intensity drops intensively at the positive electrode when applying the electric field, to only 40 % of the initial PL intensity after about 10 s. After that, the PL intensity recovers continuously, reaching values just above the initial value after 165 s. In the middle of the channel, the PL intensity remains relatively constant within the first 50 s and then decreases by about 15 % within approximately 10 s. Similarly, after approximately 120 seconds the intensity at the negative electrode exhibits a step-like drop by approximately 5 % within 10 seconds. These distinct intensity drops after ~50 and ~120 s in the middle and at the bottom of the channel, respectively, correspond to the dark front reaching the respective channel position (also see Fig. S6).

In previous work, the occurrence of a reduced PL intensity and the propagation of a dark front was attributed to the migration of positively charged iodine vacancies or neutral iodine Frenkel defects towards the negatively charged electrode.[51] The properties of the front reportedly depend on parameters such as the morphology of the sample, applied field, humidity, and laser intensity.[52] Li et al. analyzed the PL quenching dynamics in detail by PL microscopy and associated current measurements.[51] They consider a $MAPbI_3$

perovskite film between two electrodes that contains a certain density of positive iodine vacancies and a larger density of negative iodine interstitials, so that the perovskite can be considered as p-doped. The central element of their model is the notion that the applied voltage causes positively charged iodine vacancies to drift towards the negative electrode. This would start a local solid-state reaction that creates abundant non-radiative recombination centers.[51, 53] In this way, the drift of iodine vacancies would be associated with a reduction in radiative electron-hole recombination, and thus a reduced PL intensity. Hence, a continuously advancing dark front is associated with the drift of the iodine vacancies. In the model presented by Li et al., the velocity v of the front reduces as it propagates through the channel according to[51]

$$v(t) = \left(1 + \frac{2\gamma}{d} v_0 t\right)^{-1/2} v_0 \qquad (3)$$

Here d and t are the channel length and the propagation time. The initial velocity $v_0 = \frac{p_0}{p_1}\frac{\mu_C V}{d}$ depends on the ionic mobility μ_C, the voltage V and the initial hole density p_0 and the hole density in the dark region, p_1. The quantity γ is defined as $\gamma = \frac{p_0}{p_1} - 1$. By integrating eqn (3) over time, the temporal evolution of the distance *x* of the dark front from the positive electrode is given by:

$$x(t) = \frac{d}{\gamma}\left(\sqrt{1 + \frac{2\gamma}{d} v_0 t} - 1\right) \qquad (4)$$

The evolution of the PL intensity we observe in the powder-pressed $MAPbI_3$ in Fig. 3 qualitatively resembles that described by Li et al. for a solution-processed film, though we find a less pronounced reduction of the PL intensity. A moderate reduction rather than a full quenching of the PL intensity upon applying an electric field has also been found in other studies,[48, 54, 55] and it was reported that the dark PL front does not always advance over the whole channel.[51] Rather, the intensity contrast between the two sides of the

front fades as the front advances, in accordance with a diffusive behavior. While the reasons for this are not fully understood yet, it appears that the measurement conditions, such as illumination intensity or humidity, as well as the morphology and polycrystallinity of the perovskite influence the profile of the dark front.[52] Based on the qualitative similarity of the field-induced PL reduction that we observe compared to that reported by Li et al., we consider that the same mechanism applies.

Thus, we use the expression derived by Li et al. to analyze the data of Fig. 3a. We identify the position of the dark front using two independent approaches. First, we quantify *x(t)* by optically localizing the position of the dark front in the channel directly from the microscopy images at different times after the electric field was applied (e.g., see orange dashed lines in Fig. 3a and Fig. S6). At longer times and thus larger distances from the positive electrode, the precise determination of the front position *x* becomes more and more difficult as the stepwise reduction in PL intensity becomes less pronounced (Fig. S7). To improve the accuracy in determining the front position from our data, we exploit the signature of the front, i.e., the steep intensity reduction in the edge of the front. Therefore, we consider the integrated PL intensity in horizontal slices at the different channel positions *x* as a function of time and extract the time at which the front arrives from the inflection point of the PL intensity transient. This quantitative analysis further allows us to determine the change in relative intensity directly before and after the front passes through (see Fig. S7 for details about the analysis approach).

Fig. 3c shows the evolution of *x*(*t*), as extracted using both analysis approaches, together with the strength of relative intensity drop at a certain channel position. We fit *x(t)* in Fig. 3c using eqn (4) in the time range between 15 s and 100 s and obtain v_0 = 4.6 µm/s and γ = 8.2. Using $v_0 = (\gamma + 1)\frac{\mu_C V}{d}$, we determine the mobility of the ions as μ_C = 7.5×10^{-8} cm^2/Vs. From the Einstein relation (electrical mobility equation) $D = \mu k_B T/e$, the diffusion constant of the ions results as D_{ion} = 1.9×10^{-9} cm^2/s. This value agrees well

with the typical values derived by PL microscopy methods that are in the range of 10^{-8} - 10^{-11} cm^2/s.[56]

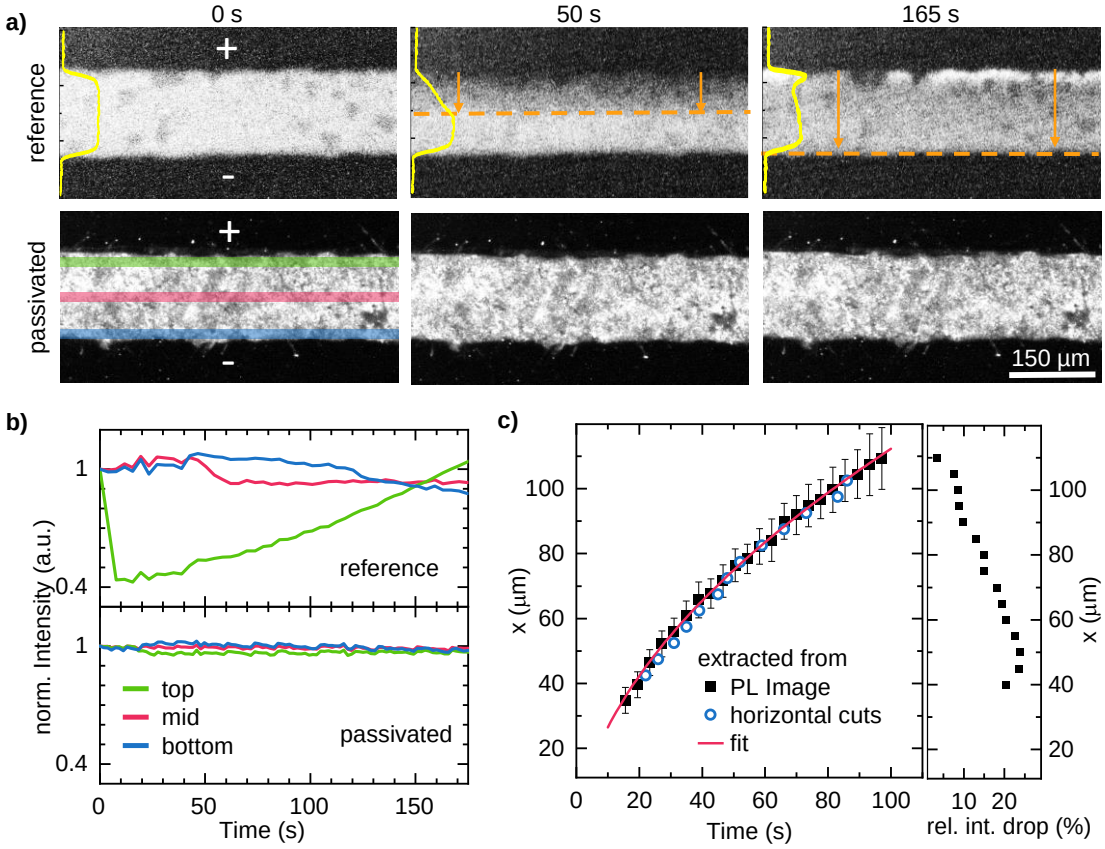

Fig. 3: (a) PL microscope images of the reference (top) and passivated (bottom) perovskite pellets (channel length 150 µm), 0 s (left), 50 s (middle) and 165 s (right) after applying an electric field of 67 V/cm and with an illumination intensity of 42 mW/cm². The plus and minus signs indicate the polarization of the gold electrodes (dark area at the top and bottom). In the reference sample, a dark front advances from the positive to the negative electrode, with its position is indicated with orange dashed lines. To the left of each PL image of the reference pellet, a vertical cross-section of PL intensity is indicated (yellow). (b) Evolution of PL Intensity at different channel positions (horizontal cross-sections), for reference (top) and passivated (bottom) pellet, normalized to their value at t = 0 s. The accumulated intensity is calculated from the green (close to the positive electrode), red (mid-channel), and blue (negative electrode) boxes shown in (a). The same area was used for the passivated and the reference sample. (c) The temporal evolution of position x of the dark front within the channel, extracted by horizontal cuts (blue circles) or directly from the PL images (black squares), together with a fit (red line) using eqn (4). The graph on the right shows the relative drop of the intensity after the dark front moves through a position x.

In contrast to the reference pellet, the passivated pellet shows no temporal change in PL intensity along the entire width of the channel and over the entire measurement period of 165 s. In particular, we do not observe any PL quenching, formation of a dark PL front (Fig. 3a), or intensity dynamics directly at the electrode (Fig. 3b). This is consistent with observations from Bai et al., where passivation of solution-processed halide perovskite thin films using an IL led to temporally stable PL microscopy images.[28] Thus, based on our findings from the PL microscopy investigations, it becomes clear that the addition of IL in the mechanochemical synthesis of $MAPbI_3$ passivates the perovskite, which significantly reduces ion migration in the powder pellet.

Regarding the passivating meachnism, we recall that iodine migration takes place primarily through iodine vacancies, which is well supported by findings of other groups.[47, 57] We hypothesise that the role of the ionic liquid is to fill up these iodine vacancies, so that they are no longer available as pathway for iodine motion. It was suggested that the electron rich nitrogen atom of the imidazole moiety of the IL binds to positively charged defects, such as iodine vacancies.[31, 58, 59] This is supported by computer simulations[60] as well as X-ray photoelectron spectroscopy and Fourier-transform infrared spectroscopy measurements.[58] Thus, while the number of ions in the device has not been reduced, but in fact may even be enhanced through the presence of the ionic liquid, there is no pathway available for their motion as the vacancies are filled up. In addition, a motion through interstitial sites is unfavourable in the close packed perovskite structure as there is insufficient interstitial space.[57]

We now address the question of how the ion migration impacts the electrical properties of the pellet, and in particular its dark current. Therefore, we measured the IV characteristics of the reference and the passivated samples in the dark (Fig. 4a). We first measured the current when sweeping the voltage in forward direction, i.e., from -10 V to 10 V, followed by a backward scan to -10 V with the same scan rate (400 mV/s.) For the reference sample, we observed a hysteresis loop in both the negative and the positive

voltage range. We repeated the IV scans with scan rates between 0.4 V/s and 10 V/s, and found the hysteresis to become more pronounced for decreasing scan rates (Fig. S8). This is in contrast to the passivated pellet, where we could not observe any hysteresis behavior in the IV curves for all scan rates used in our experiments (Fig. 4a and Fig. S8).

The hysteresis in the IV scans of perovskite pellets with symmetrical contacts was, e.g. also found by Yang et al., who assigned it to the influence of migrating ions, notably in the form of iodine vacancies, in the pellet.[61, 62] An absence of hysteresis in the IV scans in Fig. 4a thus indicates slower ion migration in the passivated pellet. A reduced dark current also occurs in the time-dependent current measurements, where we applied 10 V to the reference and passivated pellets (Fig. 4b). The passivated pellet shows a current of 2.5 nA directly after applying the voltage, which remains quasi constant during the measurement period (Fig. 4b bottom). In contrast, when the voltage is applied to the reference pellet, we observe a significantly higher initial current of 55 nA, which further rises steeply and stabilizes after about 8 s at 73 nA (Fig. 4b top). Fitting the current rise using an exponential gives a rise time of about 1 s (Fig. S9). This time scale agrees with the typical values found in potentiostatic measurements of $MAPbI_3$ at room temperature,[27] and it was associated with ion migration processes in the perovskites.[63] The absence of this rise dynamic in the passivated sample thus further supports the deduction that the addition of the IL leads to a strong reduction of ion migration in $MAPbI_3$ and to a passivation.

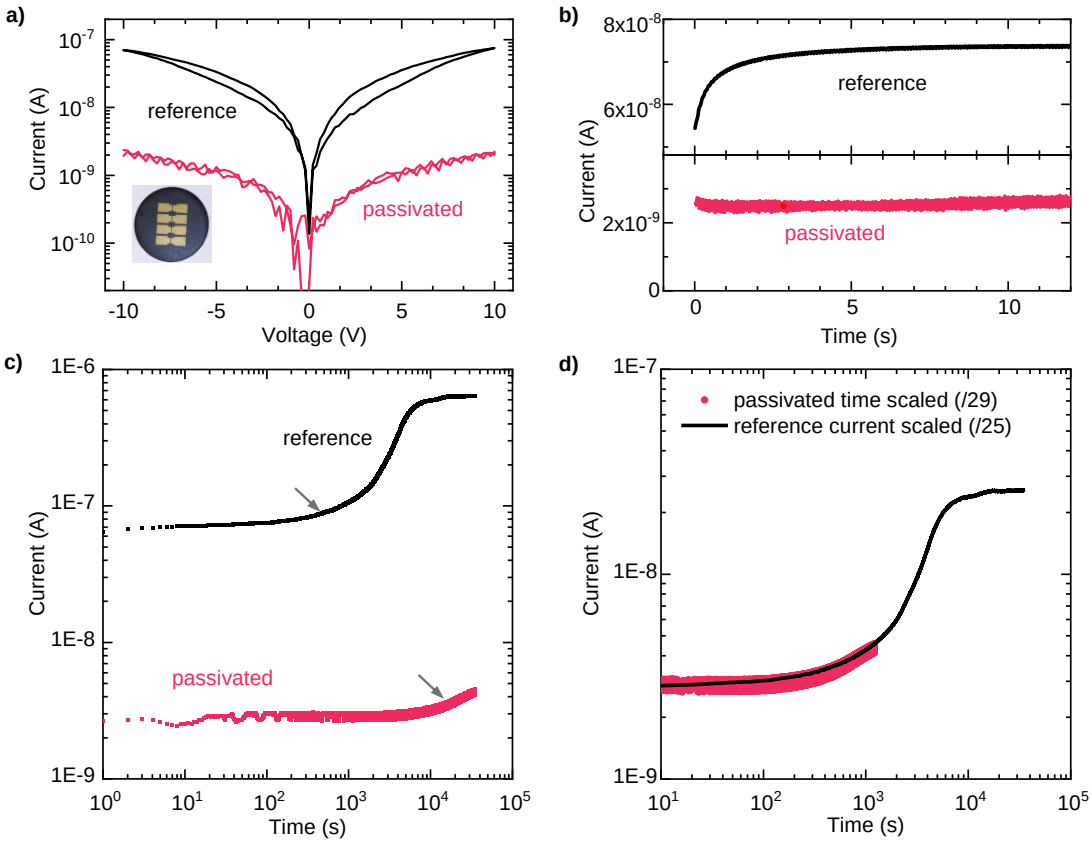

Fig. 4 (a) Current-voltage characteristics of the reference (black) and the passivated (red) pellet. The inset shows a photograph of a perovskite pellet with the lateral gold electrodes (width of 1 mm and channel length of 150 µm). (b) Temporal evolution of dark current within the first 12 s (b), and within a longer time range (c) of 36,000 s (i.e., 10 hours) upon applying a voltage of 10 V. The arrows indicate the time when the current increases considerably. (d) Same as in (c), but the reference dark current was divided by a factor of 25, while the time axis of the passivated sample was scaled by dividing by 29.

We also measured the evolution of dark current for both pellets in a nitrogen atmosphere over a longer time range of 10 hours, which is shown in a double logarithmic representation in Fig. 4c. The current of the reference pellet increases only moderately in the first 500 s under bias, then increases by almost one order of magnitude between approx. 500 s and 10,000 s, and finally approaches a constant value of approx. 6.4×10^{-7} A for the longest measured times. In contrast, the current of the passivated pellet remains

almost constant at 3×10^{-9} A within the first 10,000 s, and then starts to increase continuously to 4.4×10^{-9} after 36,000 s. It is noteworthy that, for t < 500 s, the current in the passivated pellet is reduced by a factor of 25 compared to the current in the reference pellet. Similarly, the onset of a current rise in the passivated pellet is delayed by a factor of 29 compared to the reference pellet. In fact, the two current profiles in Fig. 4c have a remarkably similar qualitative shape. This becomes evident when the current profiles are scaled accordingly in terms of both current and time (Fig. 4d). This agreement suggests that the increase in current in the passivated pellet at long times has the same physical origin as in the reference pellet. Thus, we conclude that the passivation of the $MAPbI_3$ powder with the IL does not lead to a full suppression but to a significant delay of the process causing the current drift by a factor of roughly 27±2.

A detailed analysis and interpretation of the current drifts observed here is beyond the scope of this work and will have to be addressed in the future. Nevertheless, we would like to comment on possible mechanisms that might explain our observations. Wu et al. suggested that an increase in dark current on long time scales could be associated with reactions of the migrating ions at the electrode. Such reactions would modify the electrode interface,[64] such as to facilitate charge extraction, thus increasing the current flow through the channel. Different electrochemical reactions of $MAPbI_3$ with gold that involve mobile iodide ions have been reported for voltages above 0.8 V,[65-68] independent of the perovskite thickness.[65] Considering that we applied a voltage of 10 V in our experiments, such a reaction could easily occur in our sample. The scenario for our reference pellet would then be that mobile iodine ions, traveling by a vacancy diffusion mechanism from one electrode through the perovskite channel towards the opposite electrode. This hypothesis is strengthened by the observation in Fig. 4c that the time scale, after which the main rise of the dark current occurs, i.e., about 500 s (≈ 8 minutes), agrees roughly with the time the ions need to migrate through the channel, identified as 165 s (≈ 3 minutes, Fig. 3). This hypothesis also agrees with the significantly delayed increase in current in the passivated pellet, where a reduced ion diffusion due to

passivation with the IL would result in a correspondingly delayed reaction at the electrode. It should be noted here that similar behavior was observed years ago for classical inorganic titanate perovskites that are applied for capacitors. Under applied voltages, the electrical field causes the positively charged oxygen vacancies to move from one electrode to the other, leading to a deterioration of the capacitors.[69] Higher anion vacancy concentrations, e.g., obtained by iron acceptor doping, and higher temperatures that lead to higher oxygen (vacancy) diffusion coefficients support the oxygen movement. This effect was carefully studied optically or by electrocoloration by the groups of Waser[70] and Maier,[71] respectively.

3. Conclusion

In summary, we investigated in detail the impact of adding the ionic liquid $BMIMBF_4$ to the mechanochemical synthesis of the halide perovskite $MAPbI_3$. We find that adding 1 mol% of the IL does not change the crystal structure and the morphology of the mechanochemical synthesized perovskite powder. Compared to a reference $MAPbI_3$ powder pellet, the passivated powder pellet shows, however, a reduction of the non-radiative decay rate by nearly one order of magnitude and exhibits no light soaking and PL degradation during illumination. Similarly, rise dynamics of the dark current on the time scale of 1 s, which occur in the reference pellet when applying an electrical field, are absent in the passivated pellet. This behavior is also reflected in hysteresis-free IV curves of the passivated pellet when sweeping between -10 and 10 V. PL microscopy under an electric field demonstrates that no PL darkening fronts are present within the passivated powder pellet, suggesting a significantly reduced ion migration. This reduced ion migration leads to a reduction of dark current by a factor of 25 compared to the dark current of the reference sample. Due to the reduction of ion migration, an increase of dark current on the hours-time scale, most likely due to an electrochemical reaction of the Au electrode with iodide ions, is delayed by a factor of 29 in the passivated powder

pellet. Our work thus contributes to gain a more fundamental understanding regarding how the optical and the electrical properties of powder-based perovskite thick films change by the addition of an ionic liquid.

Acknowledgment

The authors acknowledge financial support by the German National Science Foundation DFG via the projects PA 3373/3-1 and MO 1060/32-1 and GR 5505/1-1. We further thank Irene Bauer for MAI synthesis, Monika Daubinger for help with the powder synthesis, the Department of Metal and Alloys (Prof. Uwe Glatzel) for the possibility to conduct XRD measurements, the Magnetic Resonance Research Center (MRRC, Radboud University, Prof. Kentgens) for the access to the NMR spectrometer, NWO for the support of the "solid-state NMR facilities for advanced materials science", which is part of the uNMR-NL ROADMAP facility, the NMR facilitiy technicians, Gerrit Janssen, Hans Janssen and Ruud Aspers for their support, Werner Reichstein, Martina Heider, Dr. Ulrich Mansfeld and the KeyLab Electron and Optical Microscopy of the Bavarian Polymer Institute (BPI) for assistance with PL microscopy, SEM and EDX images and Sven Hüttner for fruitful discussions.

Conflict of Interest

There are no conflicts to declare.

Experimental section

Mechanochemical synthesis: The precursors MAI and PbI_2 (TCI Deutschland GmbH) were weighted in a stoichiometry of 1:1 (1.59 MAI and 4.61 g PbI_2) and put in an 80 mL ZrO_2 milling jar containing ZrO_2 milling balls with a 10 mm diameter. Cyclohexane was added as the milling agent. For the passivated powder, additionally 1 mol% with respect to Pb atoms of $BMIMBF_4$ was added to the reactants. The milling was performed in a Fritsch Pulverisette 5/4 planetary ball mill at 400 rpm. After 5 min of milling, the rotation was paused for 20 min to cool down the jar. The procedure was repeated 10 times. The cyclohexane was removed by evaporation before the powder was sieved with a 63 μm mesh size at ambient conditions.

MAI synthesis: 28.8 ml methylamine (33 wt% in ethanol, Sigma Aldrich) were dissolved in 170 ml of ethanol under an argon atmosphere. 16 ml HI (57 wt% in H_2O, Alfa Aesar) is added dropwise within 30 min while being cooled in an ice bath and the solution is stirred overnight. The solvent is removed by a rotary evaporator and the powder is washed with ether and ether/ethanol mixture until the product is white.

Pellet pressing and gold electrodes: For pressing the pellets, 0.4 g perovskite powder was weighed and put in a 1.3 cm press tool (Maassen) between two polished hard metal press pins. The pressing was carried out in a homemade mechanical screw press. By turning a threaded rod with a handle, a pressure of 100 MPa was applied for 30 minutes, yielding free-standing thick films with a thickness of 0.8 mm. For the PL Microscopy with lateral field and the electrical measurements, four pairs of gold electrodes were evaporated with a shadow mask on the pellets. Each electrode pair forms a 150 μm long channel with a width of 1.0 mm. Gold was evaporated with a rate of 0.02 nm/s until an electrode thickness of 100 nm was reached.

XRD characterization: The structural characterization of the perovskite powders was carried out by reflection mode XRD using a Bruker D8 Discover A25 with Cu $K_{\alpha I}$ radiation (λ = 0.15406 nm), whereby the $K_{\alpha II}$-rays are removed by a Ge-$K_{\alpha I}$-monochromator. The device is operated at 40 kV and 40 mA. The diffractograms were recorded in the 2θ range from 10° to 45° with a 2θ step size of 0.016°.

SEM and EDX characterization: Powders and pellets were mounted on a standard sample holder by conductive adhesion graphite-pads (Plano) and sputtered with 1.5 nm platinum. The morphology was characterized by SEM using a Zeiss Leo 1530 instrument (FE-SEM with Schottky-field-emission cathode, In-lens detector and SE2 detector) using an accelerating voltage between 3.0 kV and 20 kV. For the EDX characterization, the

pellets were vapor-coated with carbon and an EDS UltraDry SDD Thermo Fisher Noran detector was used.

Solid-state NMR spectroscopy: NMR spectra were recorded on a Varian VNMRS system operating at a magnetic field strength of 20.0 T (850 MHz) using a Varian 1.6 mm T3 HXY probe at room temperature. The chemical shift was referenced using adamantane for ^{1}H (1.85 ppm) as secondary reference. The 1D ^{1}H MAS NMR spectrum was recorded at a MAS frequency of 35 kHz. The recycle delay was set to 85s to reach full relaxation (^{1}H T_1 ~ 17 s determined by ^{1}H saturation recovery experiments).

PL measurements: The time-correlated single-photon counting (TCSPC) measurements were performed with a PicoQuant MT200 system on an inverted microscope. The samples were excited with a 560 nm diode Laser (PicoQuant LDH-D-TA-560) with a frequency of 1.0 MHz and a pulse width of 68 ps. The laser beam was focused on the sample with an Olympus Objective with 4x magnification and a numerical aperture of 0.1, leading to a spot diameter of about 6 microns in the focal plane. The excitation fluence was set to 100 nJ/cm^2. The emission was filtered with a 561 nm long-pass filter and collected by a PMA Hybrid PMT 40 photomultiplier tube (PicoQuant). The signal processing was carried out by a TimeHarp 260 Pico TCSPC board (PicoQuant). On the same setup, the steady-state PL spectra were collected with a Shamrock SR163 spectrograph in combination with a Newton 970 EMCCD camera (Andor).

PL microscope measurements with lateral electrical field: The time-dependent PL measurements with an applied electric field were carried out on a Zeiss Axio Imager.A2m microscope. The excitation in the range of 380 nm to 427 nm was applied by the microscope LED light, which was filtered with a 440/SP HC short-pass filter and an HC BS 484 imaging beam splitter (both AHF Analysentechnik AG). The light was focused with a 10x Objective (Zeiss). The excitation intensity was about 42 mW/cm^2. The PL emission was filtered by a 458 LP Edge Basic long-pass filter (AHF) and collected with a pco.pixelfly usb camera (PCO AG). A bias of 10 V at the gold electrodes was applied by a Keithley 236 source meter.

Electrical Measurements: The current-voltage characteristics, as well as the current versus time curves, were recorded in the dark and under a nitrogen atmosphere using a Keithley 2450 source meter. For the I-V characteristics a voltage-sweep from -10 V to 10 V to -10 V was used with a voltage step of 200 mV and a holding time of 500 ms before each current measurement. For the current versus time measurements, a constant voltage of 10 V was applied.

References

1. J. Y. Kim, J.-W. Lee, H. S. Jung, H. Shin and N.-G. Park, *Chem. Rev.*, 2020, **120**, 7867-7918.
2. K. Ji, M. Anaya, A. Abfalterer and S. D. Stranks, *Adv. Opt. Mater.*, 2021, DOI: https://doi.org/10.1002/adom.202002128, 2002128.
3. Y. Su, W. Ma and Y. M. Yang, *J. Semicond.*, 2020, **41**, 051204.
4. G. Kakavelakis, M. Gedda, A. Panagiotopoulos, E. Kymakis, T. D. Anthopoulos and K. Petridis, *Adv. Sci.*, 2020, **7**, 2002098.
5. Y. Zhou, J. Chen, O. M. Bakr and O. F. Mohammed, *ACS Energy Lett.*, 2021, **6**, 739-768.
6. H. Wei and J. Huang, *Nat. Commun.*, 2019, **10**, 1066.
7. NREL, Best Research-Cell Efficiency Chart, https://www.nrel.gov/pv/assets/pdfs/best-research-cell-efficiencies.20200104.pdf, (accessed 30. March 2021).
8. Y. L. Song, L. Q. Li, W. H. Bi, M. W. Hao, Y. F. Kang, A. R. Wang, Z. S. Wang, H. M. Li, X. H. Li, Y. J. Fang, D. R. Yang and Q. F. Dong, *Research*, 2020, **2020**, 5958243.
9. S. Yakunin, D. N. Dirin, Y. Shynkarenko, V. Morad, I. Cherniukh, O. Nazarenko, D. Kreil, T. Nauser and M. V. Kovalenko, *Nat. Photonics*, 2016, **10**, 585-589.
10. H. Wei, Y. Fang, P. Mulligan, W. Chuirazzi, H.-H. Fang, C. Wang, B. R. Ecker, Y. Gao, M. A. Loi and L. Cao, *Nat. Photonics*, 2016, **10**, 333-339.
11. X. Zhang, F. Li and R. Zheng, *J. Mater. Chem. C*, 2020, **8**, 13918-13952.
12. S. Shrestha, R. Fischer, G. J. Matt, P. Feldner, T. Michel, A. Osvet, I. Levchuk, B. Merle, S. Golkar, H. Chen, S. F. Tedde, O. Schmidt, R. Hock, M. Rührig, M. Göken, W. Heiss, G. Anton and C. J. Brabec, *Nat. Photonics*, 2017, **11**, 436-440.
13. Z. H. Hong, D. Tan, R. A. John, Y. K. E. Tay, Y. K. T. Ho, X. Zhao, T. C. Sum, N. Mathews, F. García and H. S. Soo, *iScience*, 2019, **16**, 312-325.
14. L. Martínez-Sarti, F. Palazon, M. Sessolo and H. J. Bolink, *Adv. Opt. Mater.*, 2020, **8**, 1901494.
15. F. Palazon, Y. El Ajjouri and H. J. Bolink, *Adv. Energy Mater.*, 2020, **10**, 1902499.
16. B. Yang, W. C. Pan, H. D. Wu, G. D. Niu, J. H. Yuan, K. H. Xue, L. X. Yin, X. Y. Du, X. S. Miao, X. Q. Yang, Q. G. Xie and J. Tang, *Nat. Commun.*, 2019, **10**, 1989.
17. N. Leupold and F. Panzer, *Adv. Funct. Mater.*, 2021, **31**, 2007350.
18. S. Tie, W. Zhao, D. Xin, M. Zhang, J. Long, Q. Chen, X. Zheng, J. Zhu and W. H. Zhang, *Adv. Mater.*, 2020, **32**, 2001981.
19. R. Zhuang, X. Wang, W. Ma, Y. Wu, X. Chen, L. Tang, H. Zhu, J. Liu, L. Wu, W. Zhou, X. Liu and Y. Yang, *Nat. Photonics*, 2019, **13**, 602-608.
20. Y. Zhao, W. K. Zhou, Z. Y. Han, D. P. Yu and Q. Zhao, *Phys. Chem. Chem. Phys.*, 2021, **23**, 94-106.
21. D. Lan, *Prog. Photovoltaics*, 2019, **28**, 533-537.
22. S. Meloni, T. Moehl, W. Tress, M. Franckevičius, M. Saliba, Y. H. Lee, P. Gao, M. K. Nazeeruddin, S. M. Zakeeruddin, U. Rothlisberger and M. Graetzel, *Nat. Commun.*, 2016, **7**, 10334.
23. J.-W. Lee, S.-G. Kim, J.-M. Yang, Y. Yang and N.-G. Park, *APL Mater.*, 2019, **7**, 041111.
24. G. Y. Kim, A. Senocrate, Y.-R. Wang, D. Moia and J. Maier, *Angew. Chem., Int. Ed.*, 2021, **60**, 820-826.
25. Z. Huang, A. H. Proppe, H. Tan, M. I. Saidaminov, F. Tan, A. Mei, C.-S. Tan, M. Wei, Y. Hou, H. Han, S. O. Kelley and E. H. Sargent, *ACS Energy Lett.*, 2019, **4**, 1521-1527.
26. S. Shao and M. A. Loi, *Adv. Mater. Interfaces*, 2020, **7**, 1901469.
27. Y. Zhong, M. Hufnagel, M. Thelakkat, C. Li and S. Huettner, *Adv. Funct. Mater.*, 2020, **30**, 1908920.
28. S. Bai, P. Da, C. Li, Z. Wang, Z. Yuan, F. Fu, M. Kawecki, X. Liu, N. Sakai, J. T. Wang, S. Huettner, S. Buecheler, M. Fahlman, F. Gao and H. J. Snaith, *Nature*, 2019, **571**, 245-250.
29. P. Zhao, B. J. Kim and H. S. Jung, *Mater. Today Energy*, 2018, **7**, 267-286.
30. X. Deng, L. Xie, S. Wang, C. Li, A. Wang, Y. Yuan, Z. Cao, T. Li, L. Ding and F. Hao, *Chem. Eng. J.*, 2020, **398**, 125594.

31. M. Li, C. Zhao, Z. K. Wang, C. C. Zhang, H. K. H. Lee, A. Pockett, J. Barbé, W. C. Tsoi, Y. G. Yang, M. J. Carnie, X. Y. Gao, W. X. Yang, J. R. Durrant, L. S. Liao and S. M. Jain, *Adv. Energy Mater.*, 2018, **8**, 1801509.
32. N. K. Noel, S. N. Habisreutinger, B. Wenger, Y. H. Lin, F. Zhang, J. B. Patel, A. Kahn, M. B. Johnston and H. J. Snaith, *Adv. Energy Mater.*, 2019, **10**, 1903231.
33. N. Leupold, K. Schötz, S. Cacovich, I. Bauer, M. Schultz, M. Daubinger, L. Kaiser, A. Rebai, J. Rousset, A. Köhler, P. Schulz, R. Moos and F. Panzer, *ACS Appl. Mater. Interfaces*, 2019, **11**, 30259-30268.
34. F. Panzer, D. Hanft, T. P. Gujar, F.-J. Kahle, M. Thelakkat, A. Köhler and R. Moos, *Materials*, 2016, **9**, 277.
35. T. Meier, T. P. Gujar, A. Schönleber, S. Olthof, K. Meerholz, S. van Smaalen, F. Panzer, M. Thelakkat and A. Köhler, *J. Mater. Chem. C*, 2018, **6**, 7512-7519.
36. A. Deyko, S. G. Hessey, P. Licence, E. A. Chernikova, V. G. Krasovskiy, L. M. Kustov and R. G. Jones, *Phys. Chem. Chem. Phys.*, 2012, **14**, 3181-3193.
37. C. Witt, A. Schmid, N. Leupold, M. Schultz, J. Höcker, A. Baumann, R. Moos and F. Panzer, *ACS Appl. Electron. Mater.*, 2020, **2**, 2619-2628.
38. M. Abdi-Jalebi, Z. Andaji-Garmaroudi, S. Cacovich, C. Stavrakas, B. Philippe, J. M. Richter, M. Alsari, E. P. Booker, E. M. Hutter, A. J. Pearson, S. Lilliu, T. J. Savenije, H. Rensmo, G. Divitini, C. Ducati, R. H. Friend and S. D. Stranks, *Nature*, 2018, **555**, 497-501.
39. L. M. Herz, *Annu. Rev. Phys. Chem.*, 2016, **67**, 65-89.
40. M. B. Johnston and L. M. Herz, *Acc. Chem. Res.*, 2016, **49**, 146-154.
41. D. W. deQuilettes, K. Frohna, D. Emin, T. Kirchartz, V. Bulovic, D. S. Ginger and S. D. Stranks, *Chem. Rev.*, 2019, **119**, 11007-11019.
42. T. W. Crothers, R. L. Milot, J. B. Patel, E. S. Parrott, J. Schlipf, P. Müller-Buschbaum, M. B. Johnston and L. M. Herz, *Nano Lett.*, 2017, **17**, 5782-5789.
43. Z. Andaji‐Garmaroudi, M. Anaya, A. J. Pearson and S. D. Stranks, *Adv. Energy Mater.*, 2019, **10**, 1903109.
44. S. G. Motti, D. Meggiolaro, A. J. Barker, E. Mosconi, C. A. R. Perini, J. M. Ball, M. Gandini, M. Kim, F. De Angelis and A. Petrozza, *Nat. Photonics*, 2019, **13**, 532-539.
45. D. W. deQuilettes, W. Zhang, V. M. Burlakov, D. J. Graham, T. Leijtens, A. Osherov, V. Bulovic, H. J. Snaith, D. S. Ginger and S. D. Stranks, *Nat. Commun.*, 2016, **7**, 11683.
46. C. Li, S. Tscheuschner, F. Paulus, P. E. Hopkinson, J. Kiessling, A. Köhler, Y. Vaynzof and S. Huettner, *Adv. Mater.*, 2016, **28**, 2446-2454.
47. J. M. Azpiroz, E. Mosconi, J. Bisquert and F. De Angelis, *Energy Environ. Sci.*, 2015, **8**, 2118-2127.
48. S. T. Birkhold, J. T. Precht, R. Giridharagopal, G. E. Eperon, L. Schmidt-Mende and D. S. Ginger, *J. Phys. Chem. C*, 2018, **122**, 12633-12639.
49. J. Zhang, C. Li, M. Chen and K. Huang, *J. Phys. D: Appl. Phys.*, 2021, **54**, 044002.
50. C. Li, A. Guerrero, Y. Zhong, A. Gräser, C. A. M. Luna, J. Köhler, J. Bisquert, R. Hildner and S. Huettner, *Small*, 2017, **13**, 1701711.
51. C. Li, A. Guerrero, S. Huettner and J. Bisquert, *Nat. Commun.*, 2018, **9**, 5113.
52. X. Deng, X. Wen, C. F. J. Lau, T. Young, J. Yun, M. A. Green, S. Huang and A. W. Y. Ho-Baillie, *J. Mater. Chem. C*, 2016, **4**, 9060-9068.
53. M. Gerhard, B. Louis, R. Camacho, A. Merdasa, J. Li, A. Kiligaridis, A. Dobrovolsky, J. Hofkens and I. G. Scheblykin, *Nat. Commun.*, 2019, **10**, 1698.
54. Y.-C. Zhao, W.-K. Zhou, X. Zhou, K.-H. Liu, D.-P. Yu and Q. Zhao, *Light: Sci. Appl.*, 2017, **6**, e16243.
55. S.-G. Kim, C. Li, A. Guerrero, J.-M. Yang, Y. Zhong, J. Bisquert, S. Huettner and N.-G. Park, *J. Mater. Chem. A*, 2019, **7**, 18807-18815.
56. D. R. Ceratti, A. Zohar, R. Kozlov, H. Dong, G. Uraltsev, O. Girshevitz, I. Pinkas, L. Avram, G. Hodes and D. Cahen, *Adv. Mater.*, 2020, **32**, 2002467.
57. C. Eames, J. M. Frost, P. R. F. Barnes, B. C. O'Regan, A. Walsh and M. S. Islam, *Nat. Commun.*, 2015, **6**, 7497.

58. W. Zhang, X. Liu, B. He, Z. Gong, J. Zhu, Y. Ding, H. Chen and Q. Tang, *ACS Appl. Mater. Interfaces*, 2020, **12**, 4540-4548.
59. M. Salado, A. D. Jodlowski, C. Roldan-Carmona, G. de Miguel, S. Kazim, M. K. Nazeeruddin and S. Ahmad, *Nano Energy*, 2018, **50**, 220-228.
60. D. Yang, X. Zhou, R. Yang, Z. Yang, W. Yu, X. Wang, C. Li, S. Liu and R. P. H. Chang, *Energy Environ. Sci.*, 2016, **9**, 3071-3078.
61. T. Y. Yang, G. Gregori, N. Pellet, M. Grätzel and J. Maier, *Angew. Chem., Int. Ed.*, 2015, **54**, 7905-7910.
62. W. Tress, *J. Phys. Chem. Lett.*, 2017, **8**, 3106-3114.
63. H. Wang, A. Guerrero, A. Bou, A. M. Al-Mayouf and J. Bisquert, *Energy Environ. Sci.*, 2019, **12**, 2054-2079.
64. T. Wu, M. Ahmadi and B. Hu, *J. Mater. Chem. C*, 2018, **6**, 8042-8050.
65. R. A. Kerner, L. Zhao, S. P. Harvey, J. J. Berry, J. Schwartz and B. P. Rand, *ACS Energy Lett.*, 2020, **5**, 3352-3356.
66. R. A. Kerner, P. Schulz, J. A. Christians, S. P. Dunfield, B. Dou, L. Zhao, G. Teeter, J. J. Berry and B. P. Rand, *APL Mater.*, 2019, **7**, 041103.
67. O. R. Yamilova, A. V. Danilov, M. Mangrulkar, Y. S. Fedotov, S. Y. Luchkin, S. D. Babenko, S. I. Bredikhin, S. M. Aldoshin, K. J. Stevenson and P. A. Troshin, *J. Phys. Chem. Lett.*, 2020, **11**, 221-228.
68. Z. Xiao, Y. Yuan, Y. Shao, Q. Wang, Q. Dong, C. Bi, P. Sharma, A. Gruverman and J. Huang, *Nat. Mater.*, 2015, **14**, 193-198.
69. R. Waser, T. Baiatu and K.-H. Härdtl, *J. Am. Ceram. Soc.*, 1990, **73**, 1645-1653.
70. R. Waser, T. Baiatu and K.-H. Härdtl, *J. Am. Ceram. Soc.*, 1990, **73**, 1654-1662.
71. I. Denk, J. Claus and J. Maier, *J. Electrochem. Soc.*, 1997, **144**, 3526-3536.